



Simulations of instability in dynamic fracture by the cracking particles method

Timon Rabczuk^a, Jeong-Hoon Song^{b,*}, Ted Belytschko^b

^a Department of Mechanical Engineering, University of Canterbury, Private Bar 4800, Christchurch, New Zealand

^b Department of Mechanical Engineering, Northwestern University, 2145 Sheridan Road Rm. A210, Evanston, IL 60208-3111, USA

ARTICLE INFO

Article history:

Received 31 January 2008

Received in revised form 17 May 2008

Accepted 5 June 2008

Available online 17 June 2008

Keywords:

Dynamic instability

Microcrack branching

Microvoids

Meshfree cracking particle method

ABSTRACT

Crack instabilities and the phenomenon of crack speed saturation in a brittle material (PMMA) are studied with a meshfree cracking particle method. We reproduce the experimental observation that the computed terminal crack speeds attained in PMMA specimens are substantially lower than the Rayleigh wave speed; the computed crack speeds agree quite well with the reported experimental results. We also replicate repetitive microcrack branching along with the increased rate of energy dissipation after attainment of a critical crack speed, even in the absence of microstructural defects. We show that the presence of microdefects changes the response only a little. The computations reproduce many of the salient features of experimental observations.

© 2008 Elsevier Ltd. All rights reserved.

1. Introduction

An interesting phenomenon in dynamic crack propagation in brittle materials, first reported by Ravi-Chandar and Knauss [1,2], is the emergence of a critical crack tip speed above which the fracture energy dissipation increases dramatically. In subsequent studies, Sharon et al. [3] and Sharon and Fineberg [4] have attributed this saturation in crack speed to parasitic microcracks that emerge at an angle to the main crack. Ravi-Chandar and Knauss [1,2] (see [5] for a compendium) attributed this phenomenon to microstructural defects of the fracture zone ahead of the crack tip, in which nucleation, growth and coalescence of voids take place. They proposed that the evolution of these processes and the microscopic path instabilities provide a rate- and state-dependent character to the fracture energy.

With the rapid growth of computational power and the development of powerful new methods for modeling dynamic crack growth, it has now become possible to examine this hypothesis, at least in a rough sense, by direct numerical simulations. Most previous studies of crack propagation in PMMA have avoided the issue of microcrack instability. In Grégoire et al. [7], good agreement was obtained with experiments in PMMA without a void model at lower crack propagation speeds at which there were no instabilities. Zhou et al. [8] have proposed a rate-dependent phenomenological model that accounts for effects of the instabilities on crack speed, but does not explicitly model the crack branches.

In this paper, we use the cracking particle method [6]. Three other types of computational methods for dynamic fracture are available at this time:

- (i) The element deletion method, where the constitutive equation is constructed so that the stress is reduced to zero when the fracture criterion is met. In this method, it is imperative that the dissipated energy in the descending branch of the stress-strain curve is scaled so that the energy is equal to the fracture energy, or the method is hopelessly mesh-dependent.

* Corresponding author.

E-mail address: j-song2@northwestern.edu (J.-H. Song).

- (ii) The interelement crack models, often called cohesive zone models, where the crack path is restricted to the interelement edges (or surfaces in three dimensions). In the original formulation of Xu and Needleman [9], all elements are separated from the beginning of the simulation and the separated element edges are mechanically joined by cohesive laws. In the Ortiz and Camacho [10] approach, however, the cohesive zones are injected along element edges only when a fracture criterion is met or the element edges are contiguous to a crack tip.
- (iii) The extended finite element method (XFEM), a methodology which can model arbitrary crack geometries without remeshing. The XFEM was first developed in Belytschko and Black [11], and Moës et al. [12] and then combined with level sets in Stolarska et al. [13] and Belytschko et al. [14]; recent developments are given in [15–23].

It was noted in a recent comparative study [24] that the element deletion method was not able to predict crack branching in a structured mesh and performed poorly in modeling crack branching for an unstructured mesh. Zhang et al. [25] have made an interesting study of the crack instability problem with the interelement crack method and achieved encouraging results. However, Song et al. [24] showed for a different problem that the restriction of crack paths to specified angles in the interelement crack model can result in a rather severe underestimation of the energy dissipation.

We have not chosen XFEM for this study because the algorithm relies on level set descriptions of the crack paths. For a simulation of complicated and extensive crack patterns, the level set description is still not sufficiently robust. Instead, we use the cracking particle method, developed in [6]. This method can be viewed as a stable and consistent form of smooth-particle hydrodynamics (SPH). It avoids the tensile instability [26–28] which generally introduce large errors in SPH simulations of tensile fracture. Furthermore, it can handle nucleation and propagation of cracks in arbitrary directions, and so avoids one of the major shortcomings of interelement crack methods. It is an extension of the meshfree methods [29,30] for dynamic crack propagation [31–33].

In this paper, we examine the effects of material imperfections on crack speed in brittle materials with the cracking particle method. We show that even in the absence of imperfections, the crack speed often reaches a saturation speed and exhibits instabilities in the form of branches. Thus, while microvoids and other imperfections may play some role in the transition of crack propagation to an unsteady phenomenon with considerable branching, it appears that it is not a critical causative effect. Instead, it appears that even for relatively homogeneous materials, extensive crack branching and the attainment of a critical speed for below the Rayleigh wave speed are quite intrinsic to crack propagation in brittle materials.

The paper is organized as follows. In Section 2, we will briefly review the meshfree cracking particle method and in Section 3, simulations of dynamic crack propagation in a brittle material are reported. We conclude this section by noting that the relations between microcrack branching terminal crack speed and increased rate of energy dissipation. Section 4 gives our conclusions.

2. Review of the cracking particles method

The cracking particle method can easily and naturally handle complicated patterns of microcrack evolution since the crack geometry is described by a set of cracked particles; we do not need to provide a representation of the crack geometry. The crack is modeled by a set of discrete cracks as shown in Fig. 1b, which compares it to a pattern of microcrack branching observed in [34]. Note that the discrete cracks are restricted to be centered on the particles, i.e. each crack plane always passes through a particle.

The basic idea of the cracking particle method is based on a decomposition of the displacement field into continuous and discontinuous parts:

$$\mathbf{u}(\mathbf{X}, t) = \mathbf{u}^{\text{cont}}(\mathbf{X}, t) + \mathbf{u}^{\text{enr}}(\mathbf{X}, t) \quad (1)$$

where \mathbf{X} are the material coordinates, t is the time, and \mathbf{u}^{cont} and \mathbf{u}^{enr} denote the continuous and the discontinuous parts of the displacement field; the latter is also called the enrichment.

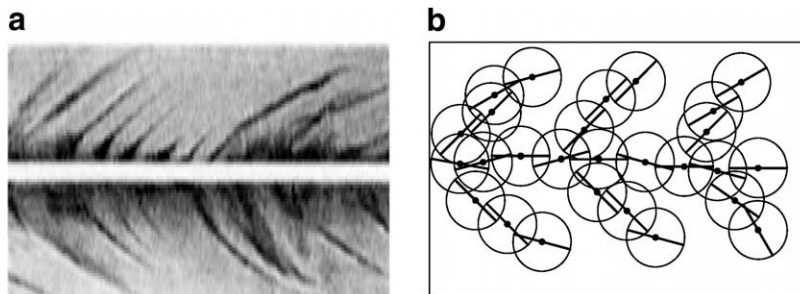


Fig. 1. A schematic representation of cracking particle method: (a) a typical pattern of microcrack branching [34] and (b) an equivalent crack path with the cracking particle method; solid circles denote cracking particles.

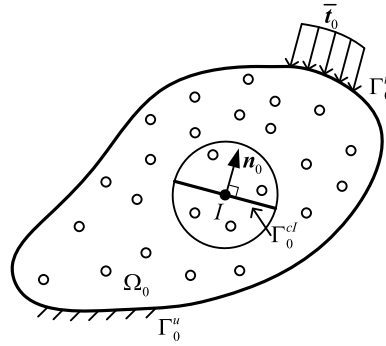


Fig. 2. Schematic representation of an initial domain with a cracking particle: solid and hollow circles denote cracking and continuous particles, respectively.

Consider a domain, Ω_0 , which contains a typical crack surface, Γ_0^c , as shown in Fig. 2. Let \mathcal{N} be the total set of nodes in the discrete model and \mathcal{N}_c be the set of cracked nodes. To model the discontinuous displacement fields, the test and trial functions are enriched with the sign function, $S(\xi)$, which is parametrized by \mathbf{q}_I . Note that only cracked nodes are enriched. The approximation of the displacement field then is given by the discrete form of (1):

$$\mathbf{u}^h(\mathbf{X}, t) = \sum_{I \in \mathcal{N}} \Phi_I(\mathbf{X}) \mathbf{u}_I(t) + \sum_{I \in \mathcal{N}_c} \Psi_I(\mathbf{X}) S(f_I(\mathbf{X})) \mathbf{q}_I(t) \quad (2)$$

where $\Phi_I(\mathbf{X})$ and $\Psi_I(\mathbf{X})$ are shape functions for the continuous and the discontinuous parts, respectively, and $f_I(\mathbf{X})$ is given by

$$f_I(\mathbf{X}) = \mathbf{n}_0 \cdot (\mathbf{X} - \mathbf{X}_I) \quad (3)$$

where \mathbf{n}_0 is the normal to the crack in the reference configuration. The sign function $S(\xi)$ is defined as:

$$S(\xi) = \begin{cases} 1 & \forall \xi > 0 \\ -1 & \forall \xi < 0 \end{cases} \quad (4)$$

In addition to the jump discontinuity function, we applied the visibility criterion with Γ_0^{cl} as opaque discs in the computation.

The discrete momentum equation is given by (see [35])

$$\mathbf{M}_{Ij} \cdot \ddot{\mathbf{d}}_j = \mathbf{f}_I^{\text{ext}} - \mathbf{f}_I^{\text{int}} \quad (5)$$

where \mathbf{d}_j is the nodal displacement which is given by $\mathbf{d}_j = [\mathbf{u}_j, \mathbf{q}_j]^T$, and \mathbf{M}_{Ij} is the consistent mass matrix. The mass matrix is diagonalized by a row-sum technique except for the mass terms associated with the cracking particles; for the cracking particles, we used block diagonal mass matrices. The vector $\mathbf{f}_I^{\text{ext}}$ is the external nodal force vector and given by

$$\mathbf{f}_I^{\text{ext}} = \begin{Bmatrix} \mathbf{f}_I^{u,\text{ext}} \\ \mathbf{f}_I^{q,\text{ext}} \end{Bmatrix} \quad (6)$$

$$\mathbf{f}_I^{u,\text{ext}} = \int_{\Omega_0 \setminus \Gamma_0^c} \varrho_0 \mathbf{b} \Phi_I(\mathbf{X}) d\Omega_0 + \int_{\Gamma_0^f} \bar{\mathbf{t}}_0 \Phi_I(\mathbf{X}) d\Gamma_0$$

$$\mathbf{f}_I^{q,\text{ext}} = \int_{\Gamma^c} 2\Psi_I(\mathbf{X}) \cdot \mathbf{n} (\tau_c + \alpha \mathbf{n} \cdot \dot{\mathbf{q}}_I) d\Gamma + \int_{\Omega_0 \setminus \Gamma_0^c} \varrho_0 \mathbf{b} \Psi_I(\mathbf{X}) S(f_I(\mathbf{X})) d\Omega_0 + \int_{\Gamma_0^f} \bar{\mathbf{t}}_0 \Psi_I(\mathbf{X}) S(f_I(\mathbf{X})) d\Gamma_0 \quad (7)$$

where ϱ_0 is the initial mass density, \mathbf{b} are body forces, \mathbf{n} is the crack normal vector, and τ_c and α are cohesive traction and damping factor, respectively. Note that the cohesive traction across the crack is treated in the RHS first term of $\mathbf{f}_I^{q,\text{ext}}$. The vector $\mathbf{f}_I^{\text{int}}$ is the internal nodal force vector and given by

$$\mathbf{f}_I^{\text{int}} = \begin{Bmatrix} \mathbf{f}_I^{u,\text{int}} \\ \mathbf{f}_I^{q,\text{int}} \end{Bmatrix} \quad (8)$$

$$\mathbf{f}_I^{u,\text{int}} = \int_{\Omega_0 \setminus \Gamma_0^c} \nabla_0 \Phi_I(\mathbf{X}) \cdot \mathbf{P}(\mathbf{X}) d\Omega_0$$

$$\mathbf{f}_I^{q,\text{int}} = \int_{\Omega_0 \setminus \Gamma_0^c} \nabla_0 \Psi_I(\mathbf{X}) \cdot \mathbf{P}(\mathbf{X}) S(f_I(\mathbf{X})) d\Omega_0 \quad (9)$$

The Rankine criterion is used to determine the onset of fracture. Subsequent to nucleation of a crack, the motion at a cracked particle is governed by a cohesive model. In this study, a linear cohesive crack model is used as shown in Fig. 3. The cohesive model is constructed so that the energy dissipated due to the crack propagation equals the fracture energy:

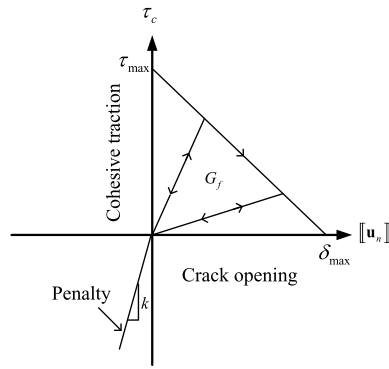


Fig. 3. Schematic of the cohesive law: the area under curve is the fracture energy, G_f . Note that the penalty can be omitted when crack deactivation is used.

$$G_f = \int_0^{\delta_{max}} \tau_c(\delta_n) d\delta = \frac{1}{2} \tau_{max} \delta_{max} \tag{10}$$

where G_f is the fracture energy, τ_{max} is the traction across the crack at fracture, δ_{max} is the crack opening displacement at which the cohesive traction vanishes, and δ_n is the jump in the displacement normal to the crack:

$$\delta_n = \mathbf{n} \cdot \llbracket \mathbf{u}(\mathbf{x}) \rrbracket_{\mathbf{x} \in \Gamma^c} \tag{11}$$

In this method, τ_{max} and δ_{max} are not fixed parameters. τ_{max} is set to the traction across the crack at the time of fracture and δ_{max} is computed from Eq. (10) based on a given fracture energy G_f and the computed τ_{max} at failure. Unless τ_{max} is equal to the traction at failure, the cohesive traction does not satisfy time continuity and may lead to substantial noise; see [36].

As shown in Fig. 3, a penalty force was added when the crack opening is negative, i.e. when the crack surfaces overlap. The penalty parameter k is two to three order magnitudes greater than the product of Young’s modulus and particle spacing. An alternative to the penalty is to simply deactivate the extra degrees of freedom at the cracking particle if the crack opening at the particle becomes negative; this is easily implemented.

3. Simulations of dynamic fracture instabilities

A series of computations were made with different sizes of PMMA specimens with an initial notch centered on the left vertical boundary as shown in Fig. 4; descriptions of the experiments can be found in [37,38,34,3,39,4,40]. In this study, we considered 380×440 mm and 380×220 mm PMMA specimens; henceforth, we call the 380×440 mm and the 380×220 mm specimens the *large* and the *small* specimen, respectively.

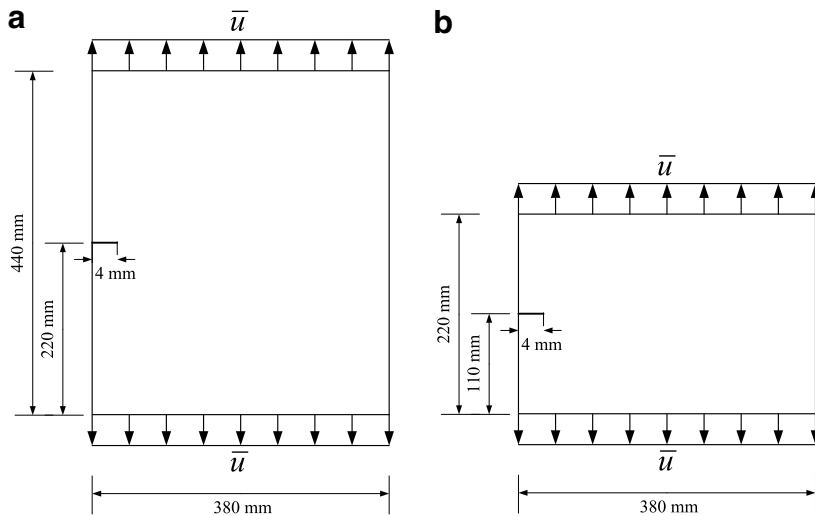


Fig. 4. Problem set-up for edge-cracked PMMA specimens under quasi-static displacement control: (a) a 380×440 mm PMMA specimen and (b) a 380×220 mm PMMA specimen.

In the experiments, the specimens were loaded by very slowly increasing the displacements of the top and the bottom surfaces [4]; the displacements were increased every 10–20 s so that the elastic waves can be neglected and the stress states inside the specimen are in equilibrium in this stage. To mimic this procedure in the simulations, we prescribed an initial equilibrium stress state, which is just below the state needed to trigger crack propagation, by means of a static simulation. Then we switched to a dynamic explicit analysis and added another displacement increment to trigger crack propagation. In the final step of the static analysis, the crack tip stress almost reaches the fracture stress and is in equilibrium.

Based on their experiments, Sharon and Fineberg [4] concluded that there are two distinct stages in the evolution of the crack. The first stage is below the critical crack speed of about $0.4v_R$, where v_R is the Rayleigh wave speed; for the PMMA material, the Rayleigh wave speed is 930 m/s. In this stage, only one main crack is formed and crack speed oscillations rarely occur. In the second stage, after the critical speed is attained, many parasitic microcracks are formed around the main crack and the crack speed manifests severe oscillations. However, the average crack speed seems to reach a stable plateau, i.e. the average crack speed saturates.

The typical pattern of microcrack branching varies with the crack speed as shown in Fig. 5. According to the experimental observations in [34], if the crack speed is lower than the critical speed, there are no apparent microcrack branches as shown in Fig. 5a, but as the crack speed increases, the number of parasitic microcracks also increases; see Figs. 5b and c.

The material properties we used in our simulations of PMMA are: density $\rho = 1190.0 \text{ kg/m}^3$, Young's modulus $E = 3.240 \text{ GPa}$ and Poisson's ratio $\nu = 0.350$. We assumed that the fracture strain is 0.02 and the fracture energy $G_f = 500 \text{ J/m}^2$; in a quasi-static problem, the size of cohesive zone is around 0.3 mm. For the explicit dynamic simulations, we used a central difference time integration scheme with a Courant number of 0.1 for all simulations; these small time steps appear to be necessary in the original versions of our software, but later versions can use larger time steps. Plane-stress conditions are assumed.

In the numerical model, both uniform and non-uniform particle distributions were considered. In this paper, however, we only show results for unstructured particle arrangements where the distances between the particles around the fracture zone are on average given by $h_p = 0.025, 0.1, 0.2$ and 0.4 mm . In order to save computation time, we used the finer particle distribution only where the crack is expected to propagate. The total number of particles for the four models were 12,000,000, 900,000, 240,000, and 770,000, respectively; such a fine resolution is necessary in order to capture microcrack branching. In the computations considered here, we described the initial notch as a traction free surface: i.e. it is explicitly modeled by separating particles by $100 \mu\text{m}$.

In order to break the symmetry of the model (which is needed to trigger instability), we introduced a slight scatter in the failure strength of the bulk material. The failure strength at every material point in the PMMA specimen is randomly perturbed by factors of less than 5.0%: the perturbation factor at each particle is obtained from a log-normal distribution around the mean value of the strength, with a standard deviation of 2.0%. We also considered smaller scatter (between 1% and 3%) and found that the results are almost identical.

The crack propagation speed in the cracking particle method was computed as follows. The location of the crack tip is taken to be the cracked particle farthest from the notch along the horizontal axis. The advancement of the crack tip is measured every $4 \mu\text{s}$ (or $2 \mu\text{s}$ for $h_p = 0.025$ and 0.1 mm). This may cause a loss of resolution in the computed crack speed, so we do not expect to be able to reproduce high frequency oscillations observed in the experiment.

3.1. Observation of microcrack branching patterns

We first compare typical computed microcrack patterns to experimental observations [34,4]. In these studies, the issues we examined are whether:

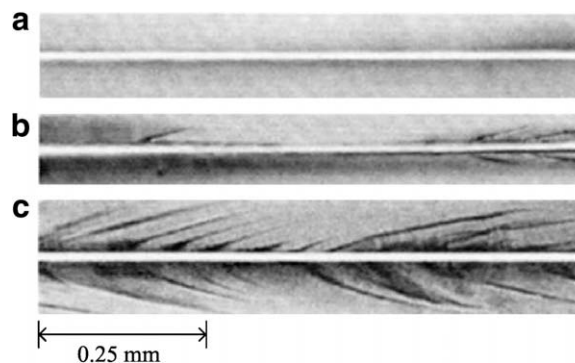


Fig. 5. A typical pattern of parasitic microcrack branching [34]: (a) crack speed, v is lower than the critical crack speed v_c ; $v < v_c$ (b) $v \simeq v_c$ and (c) $v > v_c$; for a PMMA material, $v_c \simeq 372 \text{ m/s}$.

- (i) the numerical method can capture the parasitic microcracks,
- (ii) the number of parasitic microcrack branches are increased as the crack propagation speed increases.

A typical pattern of the computed microcracks is shown in Fig. 6. In Fig. 6, only a subdomain of the specimen is shown; a scale is shown to indicate the size of the subdomain. As we can see in Fig. 6, the computations capture microcrack branching quite well and the microcrack branching is resolved better with the finer discretization. The length of the microcracks range from 0.1 to 1.0 mm. Note that even with a particle separation $h_p = 0.4$ mm, microcrack branching is clearly evident; in this case, the discretization is order of 10^{-3} of the specimen size. However, the computed pattern does not reproduce the density of cracks observed.

A straight crack growth without any microcrack branches was observed in the experiments [4] when the crack propagation speed is below the *critical crack speed*; i.e. when the crack just starts to propagate. The numerical simulations cannot capture this: the total length of initial stable crack growth is less than 0.5 cm. However, as can be seen from Fig. 7, microcrack branching in the initial stage of the crack propagation is minor. After the crack has propagated further and the crack speed exceeds the critical speed, more and longer microcracks are formed. However, we did not get a region of no branching. We surmise that in the experiment, very small branches also occurred because, as we will see, the crack speed is reproduced quite well.

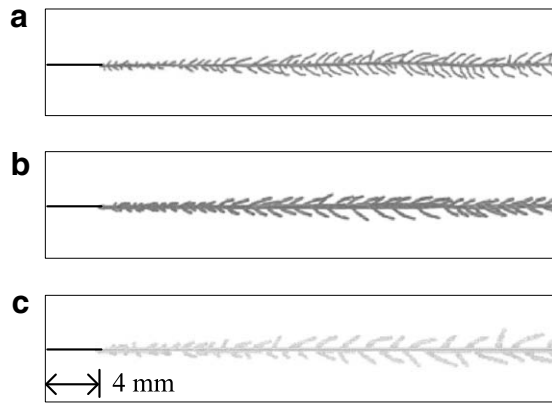


Fig. 6. The computed microcrack branching patterns in the large PMMA specimen (380 × 440 mm) with different particle separations: (a) $h_p = 0.025$ mm, (b) $h_p = 0.1$ mm, and (c) $h_p = 0.2$ mm.

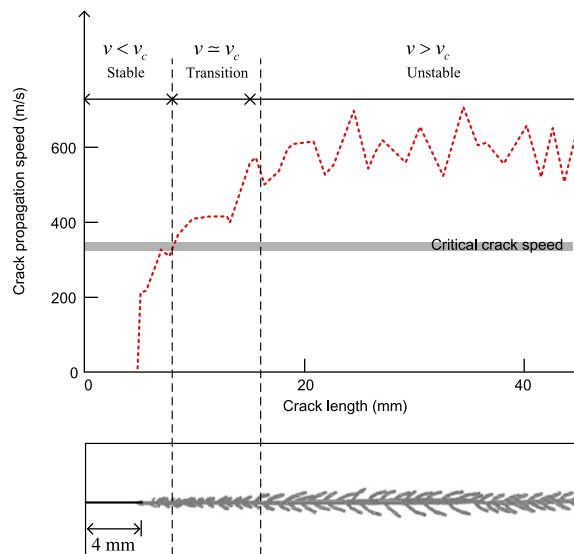


Fig. 7. The relation between the computed crack propagation speed and the computed microcrack branching in the large PMMA specimen (380 × 440 mm) with particle separation $h_p = 0.1$ mm; as the crack speed increases, parasitic microcracks are formed more frequently and they grow to larger length.

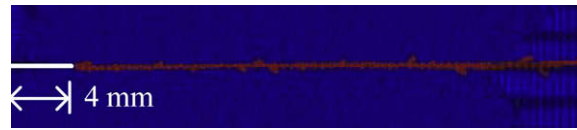


Fig. 8. The computed microcrack branching patterns in the small PMMA specimen (380×220 mm) with particle separation $h_p = 0.1$ mm; the terminal crack speed $v \approx 450$ m/s.

This transition can be seen more clearly in Fig. 8. As can be seen from Fig. 8, the crack in the small specimen is initially almost straight with few branches and in the later stages of the simulation, continues this way. The terminal crack speed, $v \approx 450$ m/s, is substantially lower than the crack speed of the large specimen, $v \approx 600$ m/s, because less elastic energy is stored in the small specimen prior to fracture.

3.2. Comparisons of crack propagation speed

We next compare the computed crack tip propagation speed and experimental results [3,4]. According to Sharon et al. [3], when the height of the specimen is decreased, the crack speed is also decreased. This is due to the fact that the stored energy in the specimen, $G = E\bar{u}^2/2L$, is inversely proportional to the specimen height, L , and the stored energy drives the crack in the displacement control setting of the experiment. In this study, we examined this by studying crack speeds in the large and the small PMMA specimens. We investigated whether:

- (i) the numerical method can capture the two distinct stages in the evolution of crack speed [4],
- (ii) the crack speed is reduced when the stored elastic energy is decreased [3].

The evolution of crack propagation speed as a function of time and crack length are shown in Fig. 9a and b, respectively. As we can see from Fig. 9b, the experimental crack speed increases to the critical speed quite smoothly. After the critical speed is attained, the crack speed manifests severe oscillations about a stable plateau. The computed crack speed also smoothly increases. The computed oscillations are much less severe; however, they increase as the model is refined. Note that longer microcrack branches are observed with the finer grids, $h_p = 0.025$ and 0.1 mm (see, Fig. 6), but the frequency of the oscillations are still much lower than those in the experiment.

In these numerical simulations, the saturation of crack speed results automatically from the evolving parasitic microcracks. In previous work by Song et al. [24] in which only a single continuous crack propagation was considered, a speed dependence was added to the fracture energy to decrease the crack speed and fit to the experimental results.

Fig. 10 compares the computed crack propagation speeds of the large and the small specimens. For the small specimen, the crack speed does not clearly reach a saturation speed as observed experimentally, but the terminal crack speed is substantially lower than the crack speed of the large specimen.

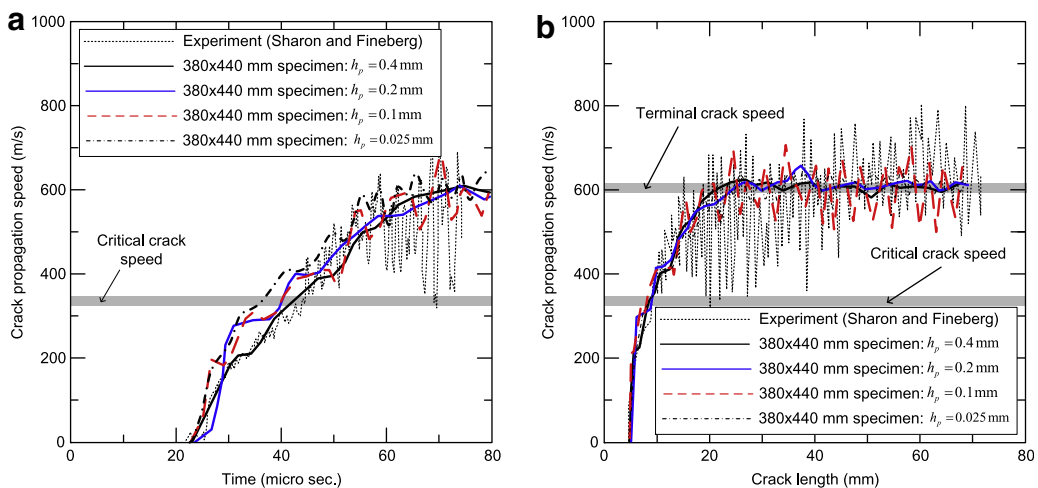


Fig. 9. Comparisons of the computed crack propagation speed with the experimental results [4] for the large PMMA specimen (380×440 mm): plot of the crack speed as a function of (a) the simulation time and (b) the crack length.

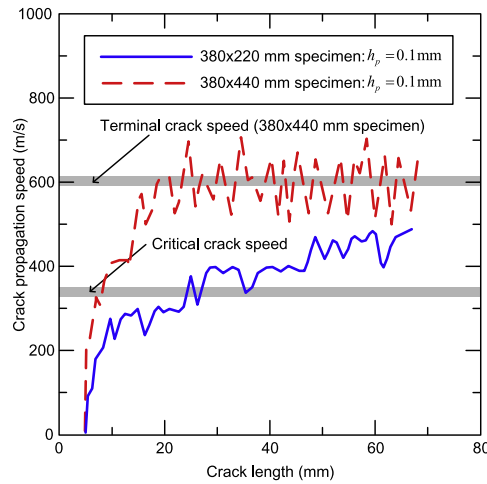


Fig. 10. Computed crack propagation speeds for the large (380 × 440 mm) and the small (380 × 220 mm) PMMA specimens.

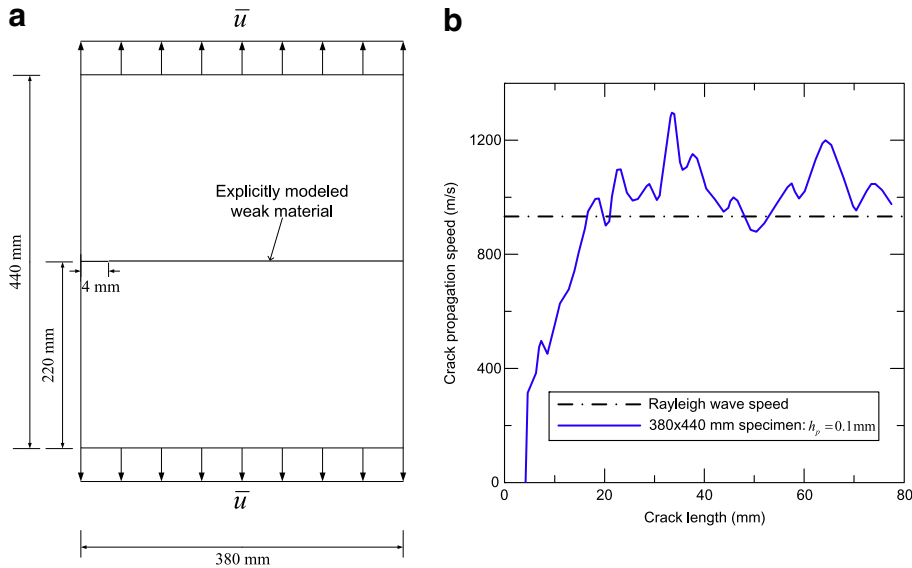


Fig. 11. (a) Problem set-up for model with a weak zone in a large PMMA specimen (380 × 440 mm) and (b) the computed crack propagation speed.

It is of interest to examine the performance of our method when the crack is confined to a straight line. We did this by reducing the thickness by 10% along a straight line ahead of the initial notch; see Fig. 11a. The computed crack speed is shown in Fig. 11b; as we expected in this simulation, the crack did not form microcrack branches. The crack speed rapidly increases up to the Rayleigh wave speed and oscillates above the Rayleigh wave speed; note that the peak crack speed is about 30% higher than the Rayleigh wave speed. This has also been observed in experiments by Needleman and Rosakis [41].

3.3. Dissipated fracture energy due to instability

The time-history of the dissipated fracture energy of the large specimen is shown in Fig. 12. As can be seen from Fig. 12a, the rate of energy dissipation suddenly increases at 36 μ s. This is due to the increased microcrack branching since more particles are cracked and consequently more energy is dissipated. Note that the crack starts to propagate around 12 μ s.

The relationship between crack speed and rate of energy dissipation can be more clearly observed by comparing the evolution of the dissipated fracture energy with the crack speed as shown in Fig. 12b. Once the crack speed exceeds the critical speed, many microcracks are formed and dissipate more energy, which slows down the crack.

As can be seen from Fig. 13, the small specimen shows a substantially lower energy dissipation due to lack of parasitic microcracks.

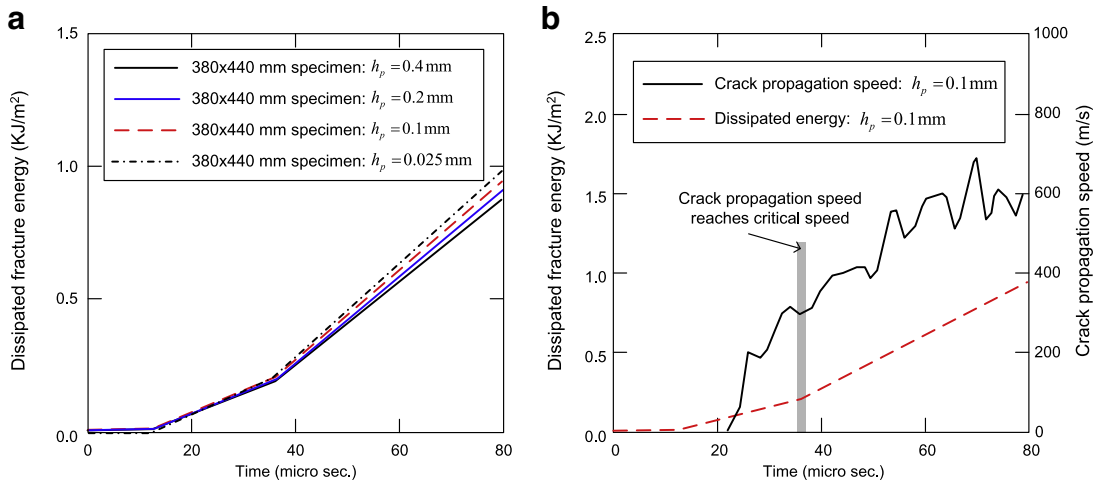


Fig. 12. Computed dissipated energy of the large PMMA specimen (380×440 mm): (a) plot of the dissipated energy as a function of time for three different refinements and (b) plot of the dissipated energy and the crack propagation speed as a function of time for particle separation $h_p = 0.1$ mm.

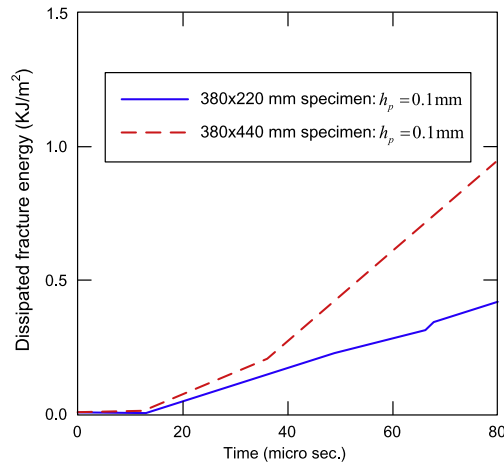


Fig. 13. Comparison of the computed dissipated fracture energy for the large (380×440 mm) and the small (380×220 mm) PMMA specimens.

3.4. Influence of microstructural defects on crack speed

In order to study the influence of microstructural defects as proposed by Ravi-Chandar and Knauss [1], we explicitly modeled pre-existing microvoids in the expected fracture zone. In every square unit cell, denoted by dashed squares in Fig. 14b, we randomly chose two particles and set the material strength equal to zero. We did this only in the domain through which we expected the crack to pass, and only particles within a certain radius of the crack tip were allowed to crack.

The crack speeds for $h_p = 0.1$ and 0.4 mm are shown in Fig. 15. The results exhibit a moderate sensitivity with respect to size and placement of the explicitly modeled microvoids, but the evolution of crack speed is almost identical to that without microvoids. The crack speeds in these models are about 13% higher than in the previous simulations without voids, and somewhat greater than the experimental crack speed. One of the notable findings is that sometimes a crack starts in front of the crack tip at the microvoids and then connects to the pre-existing main crack tip: this might also be an explanation for the oscillations of the crack speed.

4. Conclusions

We have studied unstable crack propagation in brittle materials with a meshfree cracking particle method with an emphasis on replicating the experimentally observed saturation in crack speed and microcrack branching. Such terminal crack speeds have been observed by Ravi-Chandar and Knauss [1,2] and Sharon and Fineberg [4]. Although the resolution

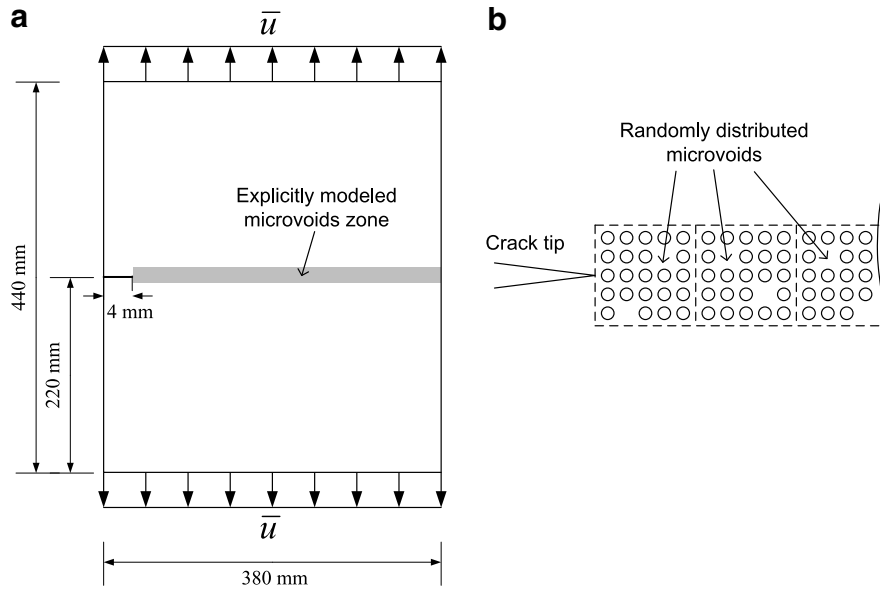


Fig. 14. (a) Problem set-up to consider microstructural defects on dynamic instabilities and (b) zoom around ahead of the crack tip in which randomly distributed microvoids are considered.

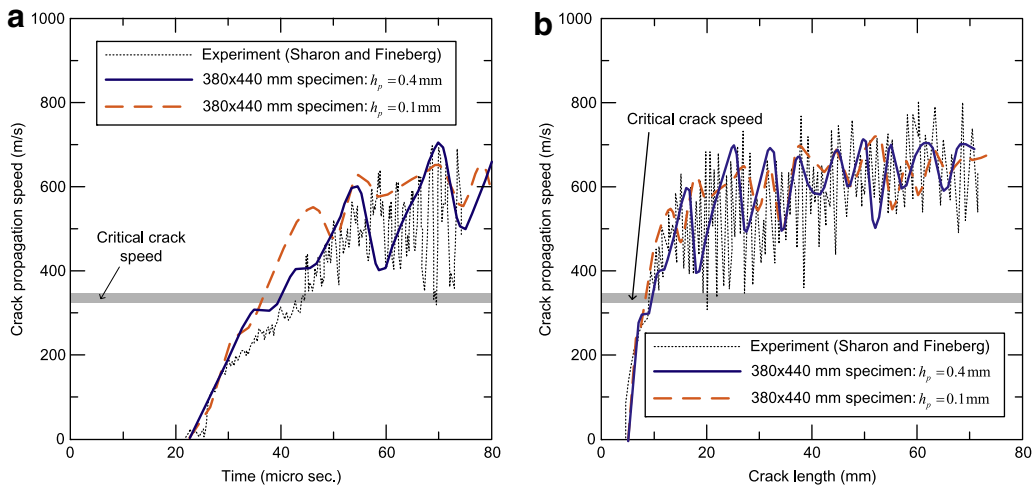


Fig. 15. Comparisons of the computed crack propagation speed with the experimental results [4]: plot of the crack speed as a function of (a) time and (b) the crack length. In the computation, randomly distributed pre-existing microvoids are considered.

of our models is not sufficient to replicate the details of the crack patterns reported by Sharon et al. [3], many of the salient features of the experiment are reproduced:

- (i) the existence of critical crack speed at which extensive microcrack branching starts,
- (ii) the attainment of a terminal crack speed significantly lower than the Rayleigh wave speed,
- (iii) the proliferation of crack branching at the higher crack speed,
- (iv) the increased rate of energy dissipation due to fracture once the terminal crack speed is attained.

The phenomenon of extensive microcrack branching occurs regardless of whether voids are included in the model (see, Figs. 6 and 16). Adding voids to the model increases the crack speed, and seems to increase the discrepancy between computation and experiment. Thus, though it cannot be conclusively established whether voids play an important role, it is apparent that a model without voids replicates most of the features observed in experiment.

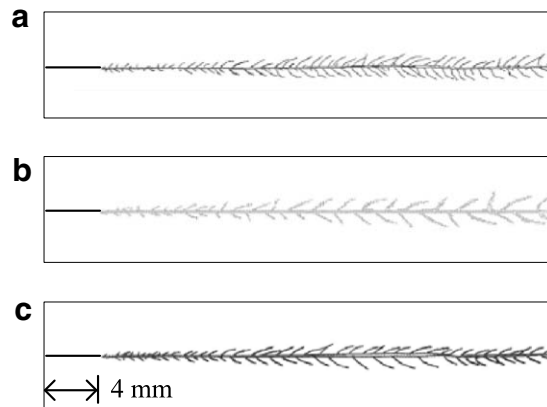


Fig. 16. The computed pattern of microcrack branching in the large PMMA specimen (380×440 mm) with different particle separations: (a) $h_p = 0.025$ mm, (b) $h_p = 0.1$ mm, and (c) $h_p = 0.2$ mm; note that in this simulation, microvoids in the fracture process zone are considered.

Acknowledgements

The support of the Office of Naval Research under Grants N00014-06-1-0380 and N00014-06-1-0505 is gratefully acknowledged.

References

- [1] Ravi-Chandar K, Knauss WG. An experimental investigation into dynamic fracture: II. Microstructural aspects. *Int J Fract* 1984;26:65–80.
- [2] Ravi-Chandar K, Knauss WG. An experimental investigation into dynamic fracture: III. On steady-state crack propagation and crack branching. *Int J Fract* 1984;26:141–54.
- [3] Sharon E, Gross SP, Fineberg J. Energy dissipation in dynamic fracture. *Phys Rev Lett* 1996;76(12):2117–20.
- [4] Sharon E, Fineberg J. Confirming the continuum theory of dynamic brittle fracture for fast cracks. *Lett Nat* 1999;397:333–5.
- [5] Ravi-Chandar K. *Dynamic fracture*. Boston: Elsevier; 2004.
- [6] Rabczuk T, Belytschko T. Cracking particles: a simplified meshfree method for arbitrary evolving cracks. *Int J Numer Meth Engng* 2004;61:2316–43.
- [7] Grégoire D, Maigre H, Réthoré J, Combesure A. Dynamic crack propagation under mixed-mode loading – comparison between experiments and X-FEM simulations. *Int J Solids Struct* 2007;44:6517–34.
- [8] Zhou F, Molinari JF, Shioya T. A rate-dependent cohesive model for simulating dynamic crack propagation in brittle materials. *Engng Fract Mech* 2005;72:1383–410.
- [9] Xu X-P, Needleman A. Numerical simulation of fast crack growth in brittle solids. *J Mech Phys Solids* 1994;42(9):1397–434.
- [10] Camacho G, Ortiz M. Computational modelling of impact damage in brittle materials. *Int J Solids Struct* 1996;33:2899–938.
- [11] Belytschko T, Black T. Elastic crack growth in finite elements with minimal remeshing. *Int J Numer Meth Engng* 1999;45(5):601–20.
- [12] Moës N, Dolbow J, Belytschko T. A finite element method for crack growth without remeshing. *Int J Numer Meth Engng* 1999;46(1):131–50.
- [13] Stolarska M, Chopp DL, Moës N, Belytschko T. Modeling crack growth by level sets in the extended finite element method. *Int J Numer Meth Engng* 2001;51(8):943–60.
- [14] Belytschko T, Moës N, Usui S, Parimi C. Arbitrary discontinuities in finite elements. *Int J Numer Meth Engng* 2001;50(4):993–1013.
- [15] Fries TP, Belytschko T. The intrinsic XFEM: a method for arbitrary discontinuities without additional unknowns. *Int J Numer Meth Engng* 2006;68:1358–85.
- [16] Menouillard T, Réthoré J, Combesure A, Bung H. Efficient explicit time stepping for the eXtended Finite Element Method. *Int J Numer Meth Engng* 2006;68:911–39.
- [17] Song JH, Areias PMA, Belytschko T. A method for dynamic crack and shear band propagation with phantom nodes. *Int J Numer Meth Engng* 2006;67:868–93.
- [18] Xiao QZ, Karihaloo BL, Liu XY. Incremental-secant modulus iteration scheme and stress recovery for simulating cracking process in quasi-brittle materials using XFEM. *Int J Numer Meth Engng* 2007;69:2606–35.
- [19] Asadpoure A, Mohammadi S. Developing new enrichment functions for crack simulation in orthotropic media by the extended finite element method. *Int J Numer Meth Engng* 2007;69:2150–72.
- [20] Prabel B, Combesure A, Gravouil A, Marie S. Level set X-FEM non-matching meshes: application to dynamic crack propagation in elastic–plastic media. *Int J Numer Meth Engng* 2007;69:1553–69.
- [21] Rabczuk T, Areias PMA, Belytschko T. A simplified meshfree method for shear bands with cohesive surfaces. *Int J Numer Meth Engng* 2007;69:993–1021.
- [22] Bordas S, Moran B. Enriched finite elements and level sets for damage tolerance assessment of complex structures. *Engng Fract Mech* 2006;73:1176–201.
- [23] Bordas S, Nguyen VP, Dunant C, Nguyen-Dang H, Guidoum A. An extended finite element library. *Int J Numer Meth Engng* 2007;71:703–32.
- [24] Song JH, Wang HW, Belytschko T. A comparative study on finite element methods for dynamic fracture. *Comput Mech*. doi:10.1007/s00466-007-0210-x.
- [25] Zhang Z, Paulino GH, Celes W. Extrinsic cohesive modelling of dynamic fracture and microbranching instability in brittle materials. *Int J Numer Meth Engng* 2007;72:893–923.
- [26] Swegle JW, Attaway SW, Heinsteinst MW, Mello FJ, Hicks DL. An analysis of smoothed particle hydrodynamics, vol SAND-93-2513. Albuquerque (NM): Sandia National Laboratories; 1994.
- [27] Swegle JW, Hicks DL, Attaway SW. Smoothed particle hydrodynamics stability analysis. *J Comput Phys* 1995;116:123–34.
- [28] Rabczuk T, Belytschko T, Xiao SP. Stable particle methods based on lagrangian kernels. *Comp Meth Appl Mech Engng* 2004;193:1035–63.
- [29] Belytschko T, Lu YY, Gu L. Element-free Galerkin methods. *Int J Numer Meth Engng* 1994;37:229–56.
- [30] Belytschko T, Krongauz Y, Organ D, Fleming M, Krysl P. Meshless methods: an overview and recent developments. *Comp Meth Appl Mech Engng* 1996;139:3–47.

- [31] Belytschko T, Lu YY, Gu L, Tabbara M. Element-free Galerkin methods for static and dynamic fracture. *Int J Numer Meth Engng* 1995;32:2547–70.
- [32] Lu YY, Belytschko T, Tabbara M. Element-free Galerkin method for wave propagation and dynamic fracture. *Comp Meth Appl Mech Engng* 1995;126:131–53.
- [33] Krysl P, Belytschko T. The element free Galerkin method for dynamic propagation of arbitrary 3-D cracks. *Int J Numer Meth Engng* 1999;44:767–800.
- [34] Sharon E, Gross SP, Fineberg J. Local crack branching as a mechanism for instability in dynamic fracture. *Phys Rev Lett* 1995;74(25):5096–9.
- [35] Belytschko T, Liu WK, Moran B. *Nonlinear finite elements for continua and structures*. New York: John Wiley & Sons Ltd.; 2000.
- [36] Papoulias KD, Sam CH, Vavasis SA. Time continuity in cohesive finite element modeling. *Int J Numer Meth Engng* 2003;58:679–701.
- [37] Fineberg J, Gross SP, Marder M, Swinney HL. Instability in dynamic fracture. *Phys Rev Lett* 1991;67:457–60.
- [38] Fineberg J, Gross SP, Marder M, Swinney HL. Instability in the propagation of fast cracks. *Phys Rev B* 1992;45:5146–54.
- [39] Sharon E, Fineberg J. Microbranching instability and the dynamic fracture of brittle materials. *Phys Rev B* 1996;54(10):7128–39.
- [40] Fineberg J, Marder M. Instability in dynamic fracture. *Phys Rep* 1999;313:1–108.
- [41] Needleman A, Rosakis AJ. The effect of bond strength and loading rate on the conditions governing the attainment of intersonic crack growth along interfaces. *J Mech Phys Solids* 1999;47:2411–49.